Proceedings World Geothermal Congress 2020+1
Reykjavik, Iceland, April - October 2021

Fracture Permeability and Saturation Effects on the Seismic Attributes of Hydrothermally Altered Rocks from a Philippine Geothermal Field

David Carlo Austria[1,2], Philip M. Benson[1], Annette E. Götz[1] and Dean S. Bullen[1]

(1) University of Portsmouth, School of Earth and Environmental Sciences, Portsmouth United Kingdom, (2) Energy Development Corporation, Pasig City, Philippines

austria.ds@energy.com.ph, philip.benson@port.ac.uk

Keywords: seismic attributes, geothermal, acoustic emission, laboratory experiment

ABSTRACT

Geophysical methods, particularly seismic attribute analysis, are seeing increased usage in studying geothermal resources in order to maximize extraction potential and minimize risks. However, to better understand deep processes it is necessary to calibrate surface seismic data to develop new models. Here, we present a series of controlled laboratory experiments where key rock physics data such as fracture network density and permeability are directly measured as a function of simulated depth. We use a suite of fresh and hydrothermally altered rocks from a Philippine geothermal field (Palinpinon or Southern Negros Geothermal Project) which are deformed using a conventional triaxial cell fitted with sensors for microseismicity, fluid pressure and fluid flow. Samples of 100mm length and 40mm diameter were prepared with small notches and a pair of offset 3mm drill holes such that once fractured, the offset drill holes form an access pathway along the newly generated fault plane. In this way, the formation and evolution of natural fracture and damage zones and resulting permeability can be directly evaluated. The sample assembly was encased in a rubber nitrile jacket to separate the sample from the confining fluid (oil) and fitted with up to 18 ports for Acoustic Emission sensors to monitor microseismicity. This setup allows an experiment to gather seismic data in different ray paths and key attributes (static and dynamic moduli) while fracture permeability develops.

Our initial results reveal a significant reduction in all seismic attributes (P/S-wave velocities and elastic moduli) after fracture development, except for Poisson's ratio, which shows the opposite trend. Further, the reduction in fracture permeability coincides with decreasing Poisson's ratio and increasing P and S wave velocities, dynamic bulk modulus, Lame's first coefficient and Young's modulus. Experiments conducted at elevated temperatures (175 °C) show a 'swarm' of Acoustic Emission events at the moment of, and shortly after, pore fluid decompression. We postulate that this is due to rapid fluid movement and phase changes from liquid to gas within the damage zone. We correlate the resulting data trends to present new links between fracture permeability and seismic data in the case of the altered andesite of the Southern Negros Geothermal Project, thus allowing for better interpretations of surface seismic models of volcanic geothermal fields in the Philippines.

1. INTRODUCTION

Seismic geophysical methods (passive and active) are commonly utilized in a range of applications, from oil and gas exploration to monitoring unrest at active volcanoes. Recently, geothermal companies such as the Energy Development Corporation (EDC) from the Philippines have adopted the use of passive seismic method in producing images of the subsurface in an effort to identify zones of importance and areas with high potential and once developed, monitor and optimise the geothermal resource (e.g. number of wells, success rate). This is achieved by integrating local/regional earthquake data using surface instruments to develop models of different seismic attributes to provide information on important reservoir properties such as permeability and fracturing (Hutchings et al., 2015). However, a limitation with this approach lies in the lack of calibration to known rock physics data at relevant pressure conditions, and to the unknown permeability at depth. In recent years, seismic methods have seen increased usage in the geothermal industry and significant steps have been made in improving the quality of models that are generated (e.g. Julian and Foulger, 2010; Hutchings et al., 2015; Zucca et al., 1994). However, in part due to the difference in the geological environment between petroleum and geothermal fields, interpreting seismic models in geothermal areas remains challenging as existing knowledge applying geophysical models to rock and fluid properties has focussed, historically, in the oil and gas sector leaving equivalent tools in geothermal areas relatively underexplored. Though established theories may be applied to a certain extent, there are still areas that need further development such as the effect of temperature to fracture development and permeability, and its relationship to seismic attributes. Further, the effects of geothermal activities such as fluid injection and production in a high temperature environment to seismicity are not well understood.

Laboratory rock physics has become a powerful tool for investigating the subsurface and has seen rapid instrument and equipment development over the past 30 years (e.g. Lockner et al., 1991; Benson et al., 2007). Topics such as deep-seated geothermal resources and crustal deformation that were previously difficult and expensive to investigate at simulated conditions are now becoming more feasible. This includes new technology that has enabled studies and experiments that better simulate subsurface conditions from volcanic to crustal level (e.g. Benson et al., 2014). Vinciguerra et al. (2005) investigated the interplay of seismic velocities, thermal cracking and permeability in Etnean Basalt by utilizing a triaxial rock physics ensemble fitted with a pore pressure permeability system. By thermally pre-stressing the materials to mimic thermal damage at depth, then subjecting samples to deformation while recording seismic data (passive and active), these experiments have demonstrated the feasibility of monitoring fracture development through their seismic response (Harnett et al., 2018). A common issue seen in reservoirs that are stimulated is permeability hysteresis, referring to the non-recovery of previously high flow rates and potentially serious for geothermal extraction. Although laboratory data on this effect is limited, for low porosity anisotropic sandstones a pressure of 90 MPa is shown to be sufficient to close permeable flow paths that did not recover (Gehne and Benson, 2017), whereas for a porous anisotropic sandstone this effect was less pronounced (Baud et al., 2012). The elastic properties of different rock types while undergoing deformation experiments have been widely studied in the past in an effort to establish relationships with fracture development (e.g. Ayling et al., 1994; Heap et al., 2009; Blake and Faulkner, 2015). The deformation of rocks can be divided into several stages, each with its own influence on the physical properties of the material. During the initial stages of triaxial deformation the increasing differential stress acting on the material closes pre-existing cracks and void spaces leading to enhancement of seismic attributes. Micro-crack closure increases Lame's first parameter, which is closely related to incompressibility (Ji et al., 2010). Conversely, during the latter stages of deformation, crack nucleation and propagation results in a reduction in seismic attributes (Ayling et al., 1994). Similarly, crack damage formation in less porous rocks also results to a significant decrease in static modulus. Cyclic stressing with progressing stress is found to generate cracks and weaken rocks (such as Etna basalt) as evidenced by the release of acoustic emissions with each cycle (Heap et al., 2009). Here, each progressive stress cycle is accompanied by an initial decrease, followed by an increase, in Young's modulus and Poisson's ratio respectively. Whilst these studies provide a useful connection between the changes in seismic attribute with fracture development, the connection of these attributes to permeability is not fully explored. It is important to establish these links as these data are key to exploring and developing energy resources in a sustainable manner. Although these studies have demonstrated the usefulness of seismic data in geothermal exploration and development, conducting more site-specific studies are needed, especially with regards to known geophysical parameters and how these change with simulated pressure (burial depth).

In this paper, we report a suite of new laboratory experiments incorporating a set of new sensors to measure both permeability and seismic attributes contemporaneously. This is important, as the use of seismic imaging such as seismic tomography is improving rapidly and opening new avenues in subsurface imaging (e.g. Julian et al., 2010; Julian and Foulger, 2010; De Siena et al., 2014; Hutchings et al., 2015). We use volcanic rocks from boreholes in the reservoir rocks of the South Negros Geothermal Production field to link the effects of fracture permeability on the measured seismic attributes as a function of pressure, simulating burial depth. In addition to the key parameter of permeability, we also report new data simulating fluid extraction at high temperatures via the induced acoustic emissions. The ability to compare laboratory seismic data to field seismicity (e.g. Benson et al., 2008; Fazio et al., 2017; Browning et al., 2016; Castagna et al. 2018) represents a useful proxy and control in inferring parameters at depth where they cannot be directly accessed. Even if this comes with a degree of uncertainty, laboratory data have been proven to be an excellent analogue of field conditions that produce qualitatively the same data, thus help calibrate field seismic methods in terms of links to important material properties and geothermal processes. Our new approach will help with the of interpreting seismic models of high temperature convective geothermal systems and understand how development of such resources contributes to the seismicity observed in the field.

2. MATERIALS, EQUIPMENT AND METHODS

2.1. Sample description and preparation

The samples utilized for this study are cylindrical sub-cores of 100mm length and 40mm diameter taken from borehole core drilled at approximately 2000m depth within the geothermal reservoir. The routine drilling activities in the Southern Negros Geothermal Project (SNGP) have allowed access to this unit, which incorporates the high temperature reservoir section. This enabled us to examine the effects of fracture permeability hysteresis and seismic attributes from a sample taken from depth, whereas the vast majority of rock physics and rock deformations studies are taken from materials from surface outcrop. The samples consist of andesite and volcaniclastics with varying porosity, density, texture and degree of alteration. The andesite is composed mainly of plagioclase feldspar and pyroxene with porosity ranging from less than 1% to 6%. As part of the available suite of samples, volcaniclastic rocks with porosity ranging from 10 to 12% were also examined.

The cylindrical cores for rock physics triaxial testing were prepared using a hollow diamond core drill, with the ends cut and ground to a parallelism of 0.01mm using a diamond-grinding wheel. A key aim of the experimental program was to attempt to generate and then assess a natural fault plane generated due to the imposition of a principal stress generating a shear fault. Similar studies have tended to use either a sawcut fault (e.g. McLaskey and Lockner, 2014; Passelègue et al., 2016) or a steel insert allowing a fault gauge to be studied (e.g. Faulkner et al., 2017). These setups have the advantage of knowing were the fault is located (as the experiment is designed with that outcome) but the disadvantage that the fault plane is not 'natural'. In the study reported here, we achieve a natural fault zone linked by offset pore fluid ports by cutting notches across the diameter at the side on both ends of the samples (Figure 1), promoting a roughly 30 degree shear fault connecting and intersecting the pore fluid ports. The notches are 2-3 mm deep and 14 mm wide while the pore fluid ports are drilled 30 mm deep and 3 mm in diameter.

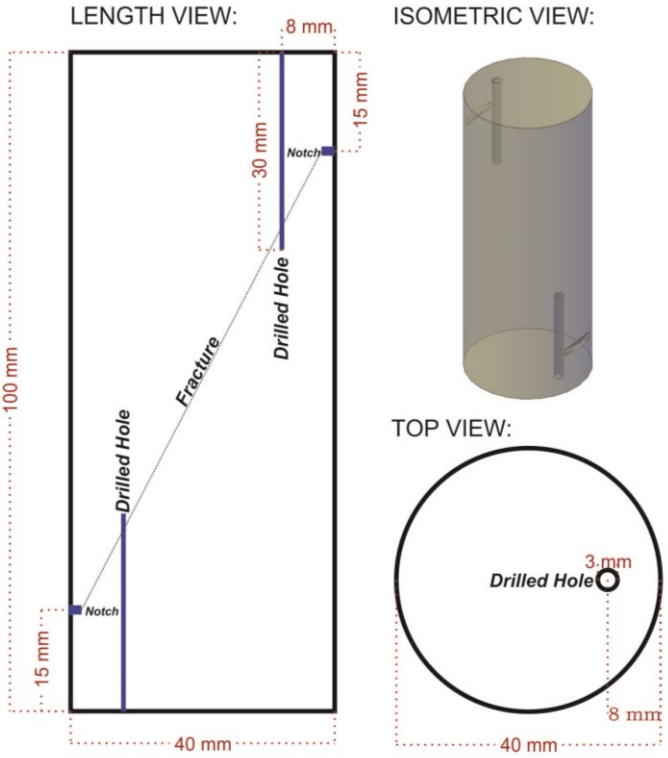

Figure 1. Schematics of the drill core where notches were cut and boreholes were drilled as part of the preparation to allow formation of a natural fracture and damage zone where permeability data are acquired.

2.2. Rock deformation equipment overview

We use a conventional triaxial deformation cell (Sanchez Technologies) comprising a 100 MPa pressure vessel fitted with an electronically compensated servo-controlled axial piston to provide a principal axial stress of up to 680 MPa (Figure 2). Confining and axial pressures are controlled using precision piston pumps with high-flash point oil as the pressurising medium. The cell is additionally fitted with two servo-controlled precision pumps providing independent upstream and downstream pore fluid (water) to the rock sample under test for flowrate data (see section 2.3 for detail). Samples are enclosed in an engineered nitrile rubber jacket to separate the confining oil in the chamber from the pore fluid. Further, the jacket has a number of ports to accept up to 18 acoustic emission (AE) sensors for recording passive micro-seismic data as the rock is deformed, and to record elastic wave (active surveys) by pulsing each sensor in sequence and receiving the resulting waveform on the remaining sensors. The AE sensors are custom-built miniature sensors consisting of 3.5 mm thick Lead-Zirconate-Titanate (PZT) piezoelectric ceramic with 1 MHz resonant frequency and a tungsten rod to reduce resonance enclosed in an aluminium casing fitted with a waveguide that seals though the engineered nitrile jacked via integral O-ring seals. The sensors convert incoming mechanical signals to electrical voltages that are then amplified by 30-70 dB and fed into two independent AE recorders for later analysis (see section 2.4 for detail). Finally, the rock physics cell includes two radial strain cantilevers and three Eddy Displacement System (EDS) sensors for axial strain, to provide volumetric strain data for static moduli. This complements the dynamic elastic moduli data as derived from the elastic wave velocity (P-wave and S-wave) data.

Two types of experiments are conducted. Firstly, a standard triaxial rock deformation experiment is performed (e.g. Fazio et al., 2017) to generate a shear fracture. This is then followed by increasing the level of effective confining pressure at hydrostatic conditions where permeability data area acquired at each step. Water flow rate (permeability) is measured by setting the pressures of the two pore fluid pumps to different pressure values and monitoring volume displacement with time. By measuring flow rate as a function of increasing confining pressure, links between the fracture damage zone, elastic wave velocities, and static moduli are then derived as a function of increasing simulated burial depth. Secondly, fracture saturation effects are investigated by inducing pore fluid phase change in the sample (water to steam), including the fracture damage zone from part (i) above, by releasing pore pressure under elevated high temperature conditions (175 °C). Simultaneous with this pore pressure release, AE data are monitored at a high sampling rate to link the acoustic emission generation via pore pressure release (or ‘venting) the pore pressure to ambient conditions.

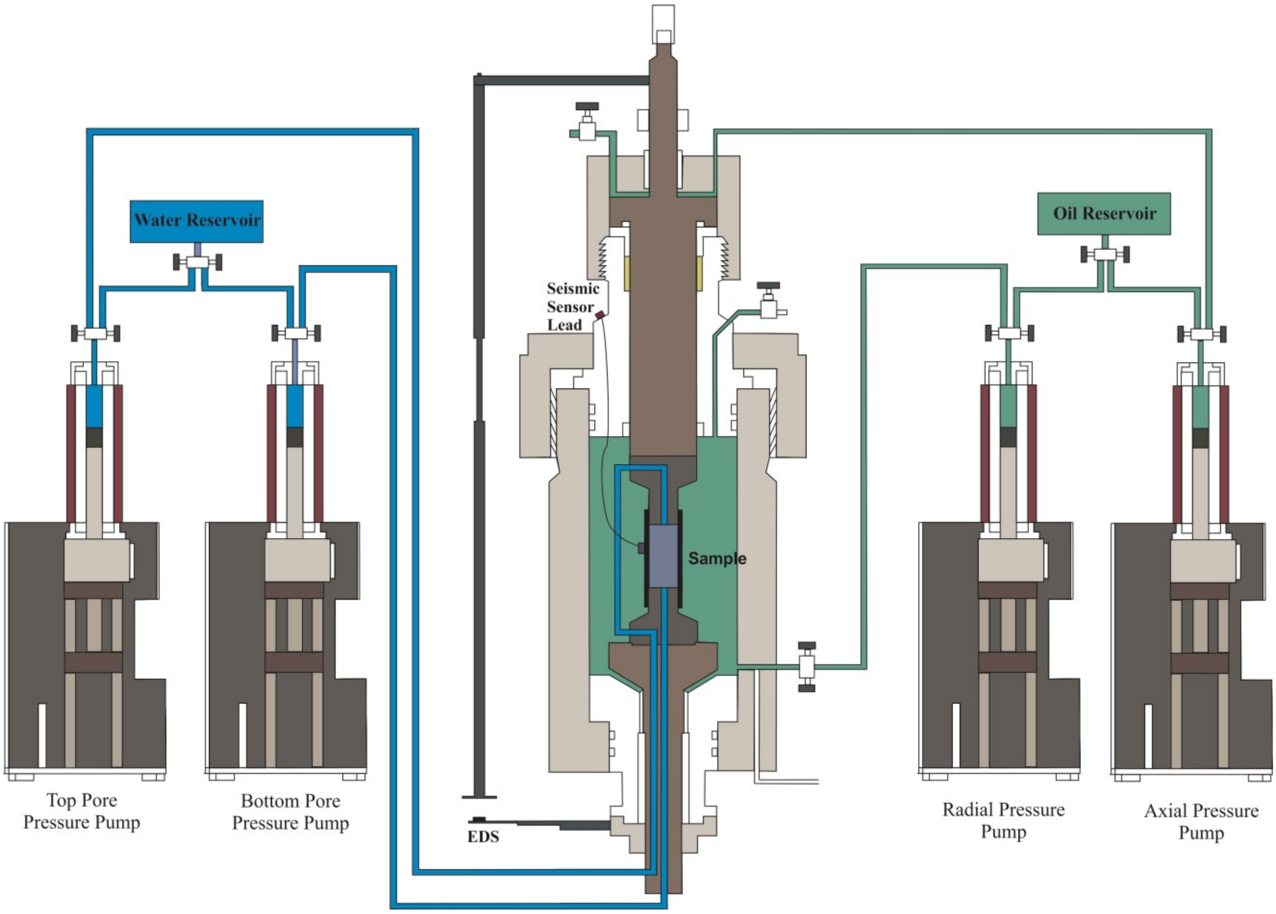

Figure 2. Schematic diagram showing the triaxial deformation equipment utilized for the study. The sample is mounted inside a rubber jacket where acoustic sensors are attached in different locations for data gathering throughout the fracture permeability experiment.

2.3. Permeability methods

We use the steady-state flow method to derive an apparent permeability based on flow-rate as measured from the change in volume with time across upstream and downstream pore pump (e.g. Gehne and Benson, 2018). Fluid flow is calculated for each step (increase or decrease) in confining pressure simulating burial depth change by allowing the upstream and downstream pumps to reach new steady states. This requires a minimum of 10 minutes to allow fluid to be expelled from void spaces when changing the effective confining pressure due to rock matrix compliance and elasticity effects. Finally, steady-state fluid flow was averaged across the two pore fluid systems (equal and opposite unless a leak is present), and then input into Darcy's equation (below) to calculate an apparent permeability of the fracture zone and bulk sample. This process is repeated across all confining pressures.

$$k = \frac{Q\,L\,\eta}{(WH)\,(P - P')}$$

where: k is permeability (m^2)
Q is volumetric flow rate (m^3/s)
L is length of the fracture zone (m)
η is the fluid viscosity at room temperature (Pa.s)
W is the width of the fracture zone (m)
H is the thickness (m)
P is the entry pore pressure (Pa)
P' is the exit pore pressure (Pa)

In order to apply Darcy's equation, we simplify the fracture zone to a rectangular prism with length, width and thickness in which the cross-sectional area is acquired. The length and width of the fracture are set at constant values given the placement of the notches and boreholes. Conversely, the height, or in this case, the thickness of the fracture zone is modeled by assigning maximum and minimum values ranging from 2 to 10 mm. These resulted to a range of permeability values for each fractured sample with varying thickness of the damaged zone. The volumetric flow rate (ml/s) is acquired from the volume change per second of both pumps while the pressure gradient is from the difference of pore fluid pressures at the bottom and top of the sample. For water viscosity, the constant value used is $8.9\text{x}10^{-4}$ Pa/s. Viscosity heavily depends on temperature but because the experiments were carried out at room temperature, the temperature is assumed to be at 25 °C.

2.4. Passive and active (elastic-wave velocities), and Dynamic moduli

Acoustic Emission data as recorded in laboratory rock physics use (e.g. Benson et al., 2007; Fazio et al., 2017), may be grouped into three types: (i) active surveys for P-wave and S-wave velocities; (ii) passive AE of finite waveform length, known as 'triggered data'; and (iii) continuous AE data, essentially the voltage from the pre-amplifiers digitized at high speed and recorded.

Active survey data are taken by pulsing each AE sensor in sequence, controlled and timed by a Pulser Interface Unit (PIU) to allow stacking of 32 traces per sensor to improve signal to noise (similar to field reflection seismic acquisition). Each sensor acts as source of signal while the remaining sensors receive, allowing signal propagation in different directions. Arrival times of both P and S waves after propagation are recorded on each sensors (of known location) allowing velocity to be calculated using the time-of-flight method (Birch, 1960). From the velocity, the dynamic moduli are calculated following the established relationship between elastic moduli and elastic wave velocities.

Passive AE data are generated from natural crack formation and fracture development while the samples are undergoing deformation, and are the laboratory proxy to field scale earthquakes (e.g. Benson et al., 2007). In this case, the mechanical energy radiated from the forming cracks and fractures is picked up by the sensors (both P and S wave sensors). Two acquisition systems operate simultaneously, taking their input from the same array of 12 AE sensors after signals are pre-amplified. The first system "Milne" records the full 12-channels of data if any one channel satisfies a pre-set amplitude threshold of 100mV in a given time window of 100us. Additional statistics are available such as the hit count per channel reflecting how many times the criterion is satisfied per second. A disadvantage of this system is the time delay needed to record the signals and re-arm for the next trigger such that a maximum of 30 events/second may be recorded.

Conversely, continuous AE data are recorded by a second "Richter" system, which avoids this pitfall by sampling AE across all 12 channels regardless if there are triggers or not. This method is capable of capturing more acoustic emissions as the harvesting and processing of the data are performed after the experiment by applying a trigger criterion in software using 'ideal' criteria, such as higher number of sensors that recorded the signal, and fine-tuning this by re-running the process as needed (e.g. Benson et al., 2007). In this way, the continuous data processing procedure filters out the noise and improves the overall quality of harvested events. Both AE systems digitise data at 10 MHz sampling rate, and 16 bit resolution. In this study, both triggered and continuous are only utilized for the fracture saturation procedure where pore pressure is intentionally dropped at high temperature conditions.

3.0. RESULTS

Based on the initial stress-strain data across all samples (Figure 3), sample AA4 (density of 2.7 g/cm^3 and porosity of 0.6 %) displays the highest strength of approximately 220 MPa differential stress. It exhibits brittle deformation upon failure with a simple shear failure plane, and a residual strength of 70 MPa. This is followed in terms of strength by sample AA1-1 and AA3 (density of 2.55 g/cm^3 and 2.68 g/cm^3, respectively). The high porosity (>10%) and low density samples (<2.4 g/cm^3), AA5 and AA6-1, which are volcaniclastic rocks, exhibit strength of around 50 to 60 MPa with noticeable post-peak ductile behaviour. Here, we report the initial analysis from samples AA4 and AA6-1 that have varying porosity (<1% and 10%) and density (2.7 and 2.45 g/cm^3) and discuss this in terms of seismic attributes while undergoing deformation.

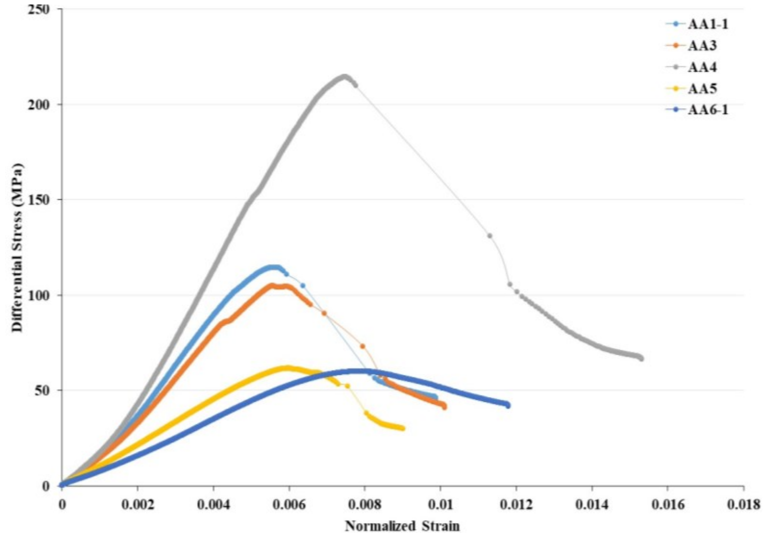

Figure 3. Stress-strain plot of volcanic rocks from Southern Negros Geothermal field under 5 MPa effective confining pressure.

3.1. Seismic attributes: andesite

The low porosity andesite sample AA4 has an initial P and S-wave velocity of 5340 m/s and 2430 m/s, respectively (Figure 4). Both velocities increase with time from 0 to 4000s. P-wave velocity data exhibit a larger rate of increase compared with S-wave wherein P-wave peaks at 5700 m/s while S-wave reaches 2500 m/s. Immediately after sample failure and shear fracture development at 4000s, velocity decreases to 4000 m/s and 1490 m/s for P-wave and S-wave respectively. The principal axial stress is then reduced to restore a hydrostatic condition of 5 MPa effective pressure, during which time velocities increase slightly to 4200 m/s for P-wave and 1500 m/s for S-wave, but maintain a positive post-peak trend with time as hydrostatic conditions are increased stepwise to 10, 20 and then 30 MPa (dotted vertical lines). At the same time, a flow rate of 0.0077 ml/s is acquired from the sample following failure, decreasing to 0.0003 ml/s at 30 MPa effective pressure where P-wave is at 5200 m/s (Figure 4A) and S-wave at 1700 m/s (Figure 4B).

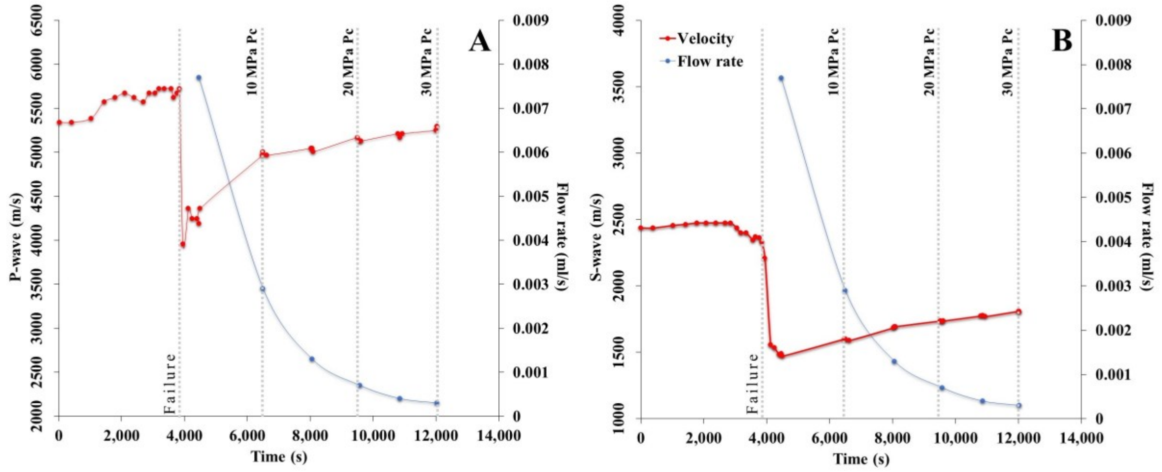

Figure 4. P and S wave velocities (red) in an andesite sample (AA4) undergoing fracture formation and damage zone development. Flow rate data (blue) acquired after failure or deformation at different effective confining pressure (Pc) is also plotted.

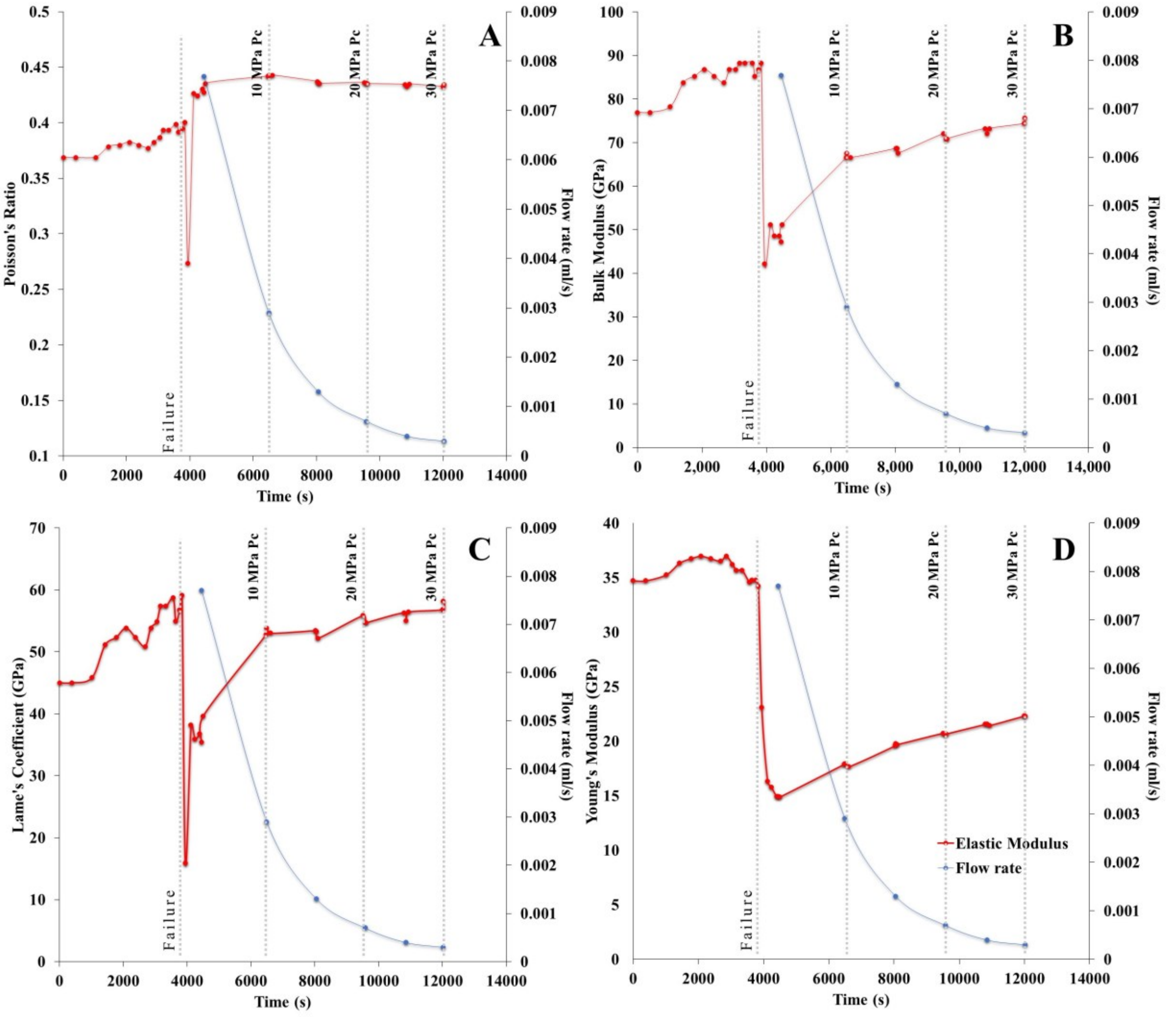

Figure 5. Dynamic modulus evolution (red) in a low porosity andesite sample AA4 while undergoing deformation and fracture development. Poisson's ratio (A), bulk modulus (B), Lame's coefficient (C) and Young's modulus (D) are plotted with flow rate data (blue) acquired after failure and following increase in confining pressure (Pc).

While the difference between P and S-wave response to changing environmental conditions is not easily observed by visually comparing trends, the use of elastic moduli may instead be used to highlight some of these variations. The relationship between P and S-wave velocities, previously utilized to study rock properties (e.g. Bonner et al., 2006; Ayling et al., 1995) provides some perspective on the state of the rock mass. Figure 5 shows the influence of fracture and damage zone development on Poisson's ratio, bulk modulus, and Young's modulus and Lame coefficient, as calculated using elastic wave velocities.

At the start of deformation, sample AA4 has a bulk modulus of 78 GPa, Young's modulus of 35 GPa, Poisson's ratio of 0.36 and Lame's coefficient of 45 GPa (Figure 5A to D). Increasing differential stress applied on the sample increases these properties to 89 GPa, 59 GPa, 37 GPa and 0.39 respectively at the point of maximum differential stress (just before 4000s). At 4000s where failure or sample deformation occurs, a noticeable decrease in all these properties is observed with the exception of Poisson's ratio, which decreases only initially before recovering to a value slightly higher than pre-failure. Bulk modulus decreases to 50 GPa at 5 MPa effective confining pressure while Young's modulus decreases to 15 GPa. Lame's coefficient also decreases from 59 to 38 GPa. Conversely, Poisson's ratio increases with failure, from 0.39 to 0.4 (Figure 5A). Under hydrostatic condition after failure, the elastic properties, bulk and Young's moduli and Lame's coefficient all show an increasing trend with increasing effective confining pressure. At 30 MPa, bulk modulus increases to 75 GPa, Young's modulus to 23 MPa and Lame's coefficient to 57 GPa.

3.2. Seismic attributes: AA6-1 volcaniclastic rock

Sample AA6-1 (of porosity >10% and density <2.45 g/cm^3), exhibits generally low values in terms of its seismic attributes. In addition, and in contrast with the sample AA4 with insufficient porosity to yield a background flow rate, a flow rate of 0.00672 ml/s was measured before deformation started, at a hydrostatic pressure of 5 MPa effective pressure. As shown in figure 6, initial P-wave velocity is measured at approximately 2500 m/s, while S-wave is at around 1450 m/s. Both velocities exhibit increasing trend in response to increasing differential stress with P and S-wave velocities reaching 2800 m/s and 1600-1700 m/s, respectively. Failure and fracture development occurs at approximately 2300s, is then marked by rapid decrease to 2520 m/s (P-wave) and 1400 m/s (S-wave), and then a gradual reduction in the wave velocities as differential stress is lowered to achieve a hydrostat, with P-wave decreasing to 2500 m/ and S-wave to 1200 m/s. At this point, flow rate has significantly increased from the background value to 0.0102 ml/s at 5MPa effective confining pressure. The subsequent increase in confining pressure post failure gradually reduces the flow rate while the elastic wave velocities exhibit a steady increase. At maximum effective confining pressure of 30 MPa, flow rate reduces to 0.005 ml/s. Contrary, P and S wave velocities increase to 3000 m/s and 1500 m/s, respectively. P-wave is also observed to reach levels higher than its pre-failure peak at 2000s (Figure 6A).

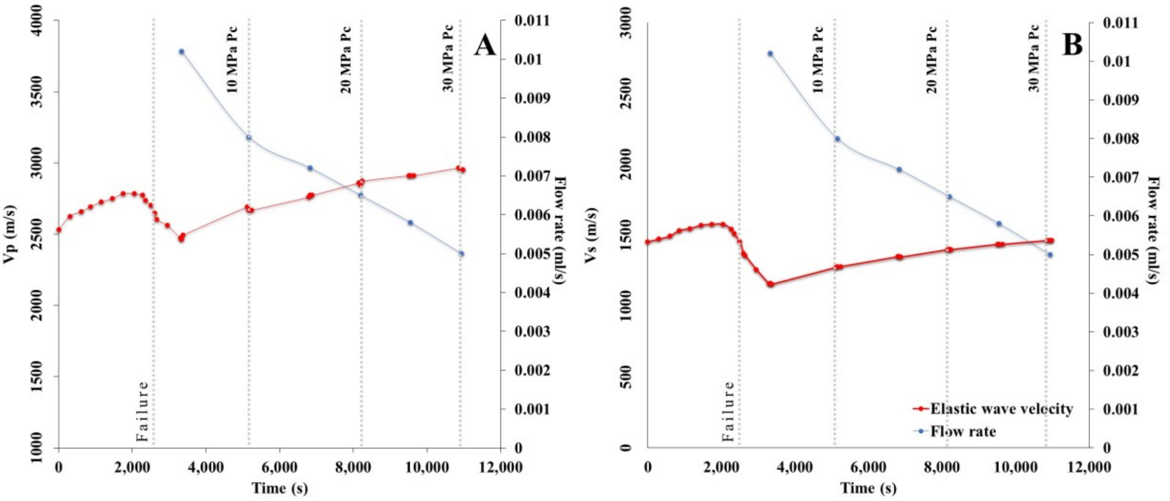

Figure 6. Elastic wave velocities showing reduction as a response to crack propagation and fracture development. Flow rate data (blue) exhibits decreasing trend with increasing confining pressure post failure.

Before deformation and shear fracture development, sample AA6-1 has an initial Poisson's ratio, bulk modulus, Lame's coefficient and Young's modulus of 15 GPa, 0.27, 8 GPa and 6 GPa, respectively. These properties, with the exception of Poisson's ratio, increase with time from 0 to approximately 2000s, marking the stage of the experiment where differential stress continuously increases. Bulk increases to 18.5 GPa while Young's modulus increases to 10 GPa. The Lame coefficient also exhibits an increasing trend reaching 7 GPa at 2000s. Conversely, Poisson's ratio slightly reduces to 0.25 at the same time. The occurrence of failure at approximately 2200s is found to significantly reduce both bulk and Young's modulus of the sample (decreasing to 14 GPa and 6.8 GPa respectively). The value of Poisson's ratio shows a significant increase from 0.25 to 0.36 after failure. Finally, as the effective stress increases from 5 to 30 MPa, the bulk modulus, Young's modulus and Lame coefficient show a steady increase similar to the response of P and S-wave. Bulk modulus exceeds 20 GPa at 30 MPa confining pressure, while both Young's and Lame coefficient increase to approximately 10 GPa. This post-failure increase in confining pressure however is observed to gradually reduce Poisson's ratio from 0.36 to 0.34.

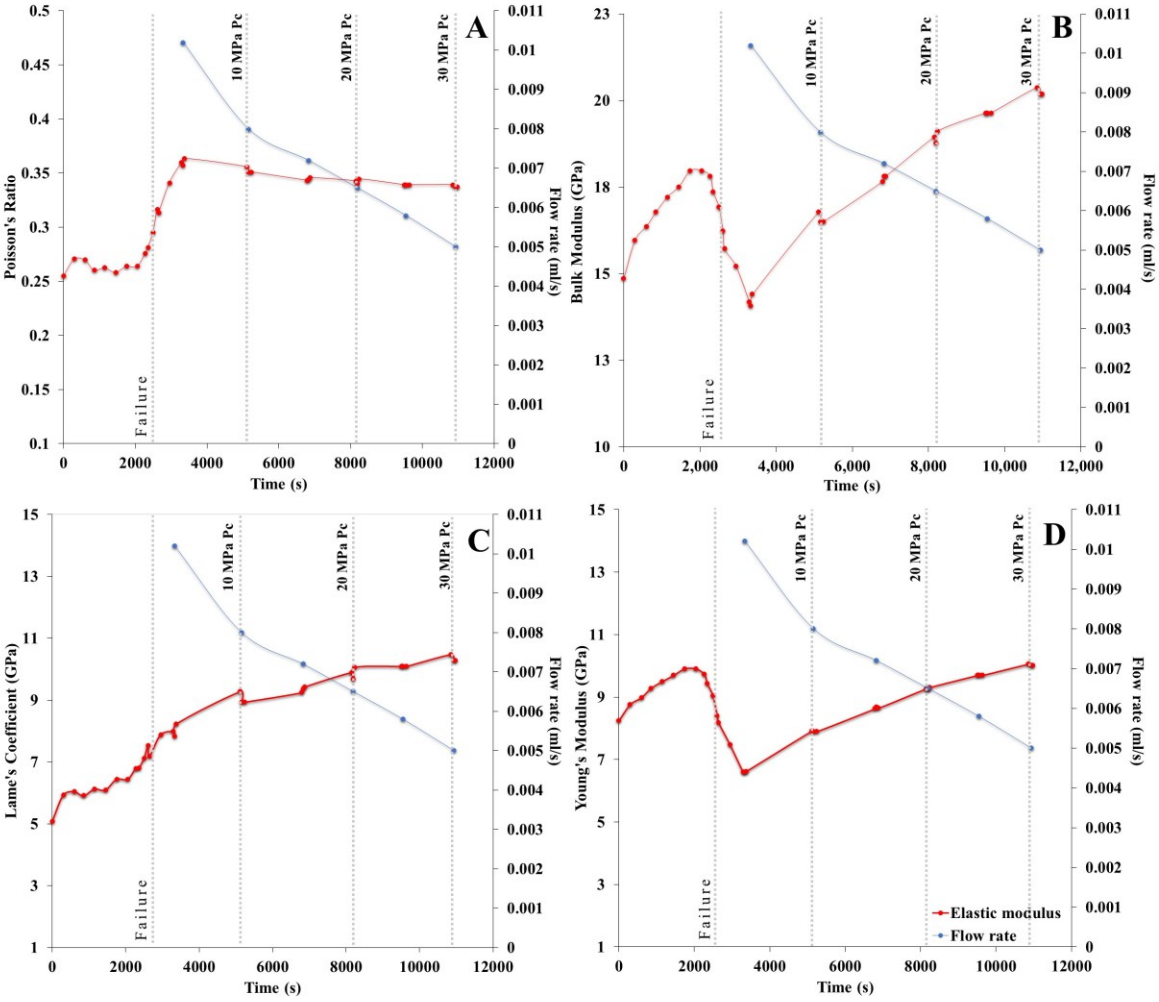

Figure 7. Dynamic moduli evolution in a highly porous AA6-1 sample while undergoing deformation and fracture development. Flow rate data is also plotted (blue). Poisson's ratio (A) showing opposite response to failure compared with bulk (B) and Young's modulu (D) and the Lame parameter (C).

3.3. Seismicity in high temperature convective geothermal systems

Using a non-porous andesite sample, AA2, the effects of changing fluid saturation within a fracture or damage zone by recording the occurrence of acoustic emission was carried out at 20 MPa confining pressure, simulating depths of around 1km (Figure 8). Acoustic emission data, axial strain and pore pressure and voltage response are shown in figure 8. At the onset of pore pressure release (from 10 to <1 MPa at 175 °C), a significant increase (or 'swarm') is measured in the AE hit rate, reaching 300 hits within a second at the point of pore pressure venting. By using one of the AE channels to record the pore pressure at a very high sampling rate (the same 10 MHz rate as for the AE data), further details are seen relating to the fluid-rock trigger generating the seismicity. Prior to venting AE hit rate is minimal from 120 to 140s. At the initial release of pore pressure (142s), a short spike in AE rate to approximately 180 hit/s is seen, during which time the pore pressure briefly remains at just under 1 MPa and AE rate decreases (Figure 9). A short time later, approximately 143s, a large and emergent increase in AE rate is seen, during which time the pore pressure finally vents to zero ambient pressure. Measurement of axial strain data does not show any movement, further suggesting the AE data are purely generated by the fluid venting and the rock-fluid coupling during the pressure release, combined during the phase change.

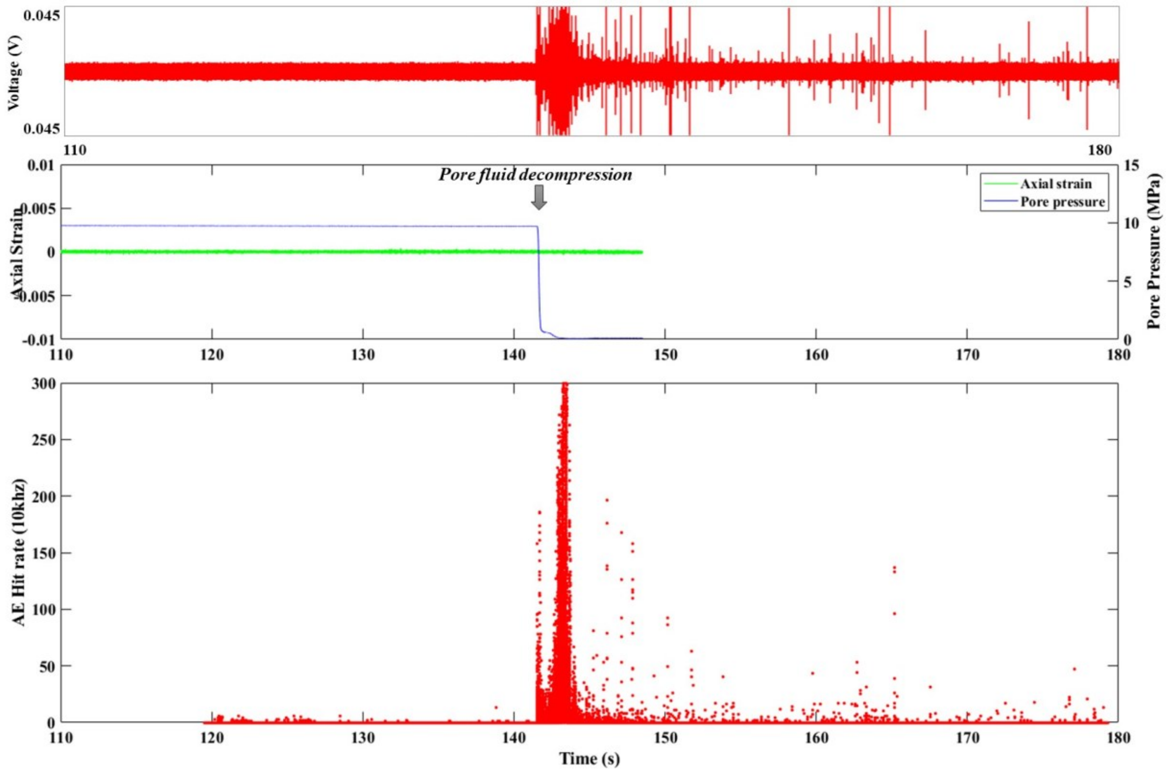

Figure 8. Acoustic emission and axial strain data acquired during pore pressure decompression at 20 MPa confining pressure and 175^{0}C temperature conditions.

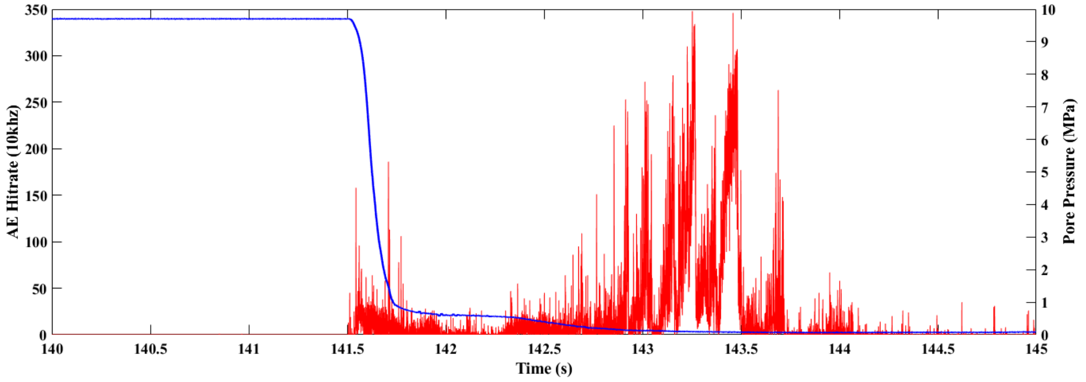

Figure 9. AE-pore pressure plot showing the time period from 140 to 145s. The pore pressure is seen briefly to remain at 0.6 to 0.8 MPa immediately after fluid decompression.

4.0. DISCUSSION AND CONCLUSION

Seismic velocities are commonly utilized to infer the state of material as a response to changing pressure and temperature conditions (e.g. Nasseri et al., 2004; Benson et al., 2008). Development of secondary structures, both macro and micro, are known to significantly influence P and S-wave velocities and are thus useful in energy resources exploration (e.g. Nara et al., 2011; Vinciguerra et al., 2015). Experiments carried out on andesite and volcaniclastic rock samples highlight the sensitivity of the seismic properties to macro and micro-crack opening and closing as a result of progressing pressure conditions. At the early stage of deformation where crack closure and compaction is dominant, P and S-waves exhibit increasing trends that suggest sample stiffening. Conversely, crack propagation leading to failure and sample deformation is marked by large reduction in velocities in both andesite and the volcaniclastic rock. We have shown here that, using P and S-wave data, other properties such as bulk modulus, Lame's coefficient, Young's modulus and Poisson's ratio are both helpful and in some cases more sensitive in providing information on the state of the material. Crack opening generally decreases these parameters, with the exception of Poisson's ratio, which increases with sample weakening likely caused by fracture development. In contrast, increasing the effective confining pressure, which simulates burial at different depths for the already deformed samples, shows a positive correlation with P and S-wave velocities and elastic properties, again with the exception of Poisson's ratio. The results of the experiments are consistent with previous studies that examined both dynamic and static moduli in different rock types subjected to high temperature and pressure conditions that result in the formation of both macro and micro fractures (e.g. Ayling et al., 1994; Heap et al., 2009; Blake and Faulkner, 2015). Young's modulus and Poisson's ratio are found to exhibit opposing trends with increasing fracture density in Etna Basalt owing to cyclic stressing (Heap et al., 2009). In addition, this decrease is often linked to thermal stressing, resulting in micro-cracks development due to differential expansion in the mineral phases, lowering P and S-wave velocities (Nara et al., 2011).

By applying different fracture thickness with the known confining pressure and flow rate, we are able to model the apparent permeability in the undeformed high porosity volcaniclastic rock at 1.4×10^{-15} m^2 at 5 MPa effective confining pressure. The formation of a fresh fracture and damage zone increases the permeability to 1.97×10^{-14} m^2 at a 2 mm fracture thickness, and ranges from 3.95×10^{-15} to 9.87×10^{-15} m^2 with a thicker damage zone (Figure 10A). Similarly, permeability in andesite increases, ranging from 3.41×10^{-15} to 1×10^{-14} m^2 at 5 MPa effective confining pressure (Figure 10B). Subsequent increase in confining pressure to 30 MPa reduces permeability in both rock types to 7.46×10^{-15} m^2 in the volcaniclastic rock and 3.41×10^{-16} m^2 in andesite. While increasing confining pressure is seen to consistently reduce permeability by closing the macro and micro-structures that allow fluid movement, a difference in the rate of decrease is noted between the samples. Permeability is found to reduce at higher rates in the deformed andesite than the volcaniclastic rock that it decreases to less than 1.5×10^{-15} m^2 at 15 MPa. This is interpreted to be due to the easily closed macro-structure or, in this case, shear fracture plane that developed in andesite. Although this also occurs in the volcaniclastic rock, the presence of higher density of microstructure as reflected in high porosity compensates for the closing of the shear fracture allowing relatively higher permeability compared with the andesite. Examination of the influence of structures to permeability in Seljadur Basalt (Nara et al., 2011) has revealed that while both macro-fractures and micro-cracks contribute heavily to permeability at low confining pressures, micro-cracks tend to dominate at higher confining pressures as macro-fractures are easily closed and restrict fluid movement (Nara et al., 2011). This supports the findings in volcanic rocks from Southern Negros Geothermal Field wherein permeability modeled at elevated confining pressures is higher in initially porous volcaniclastic rock than the deformed non-porous material. The transition in permeability in which microstructures starts to take control appears to occur from 10 MPa to 15 MPa effective confining pressure.

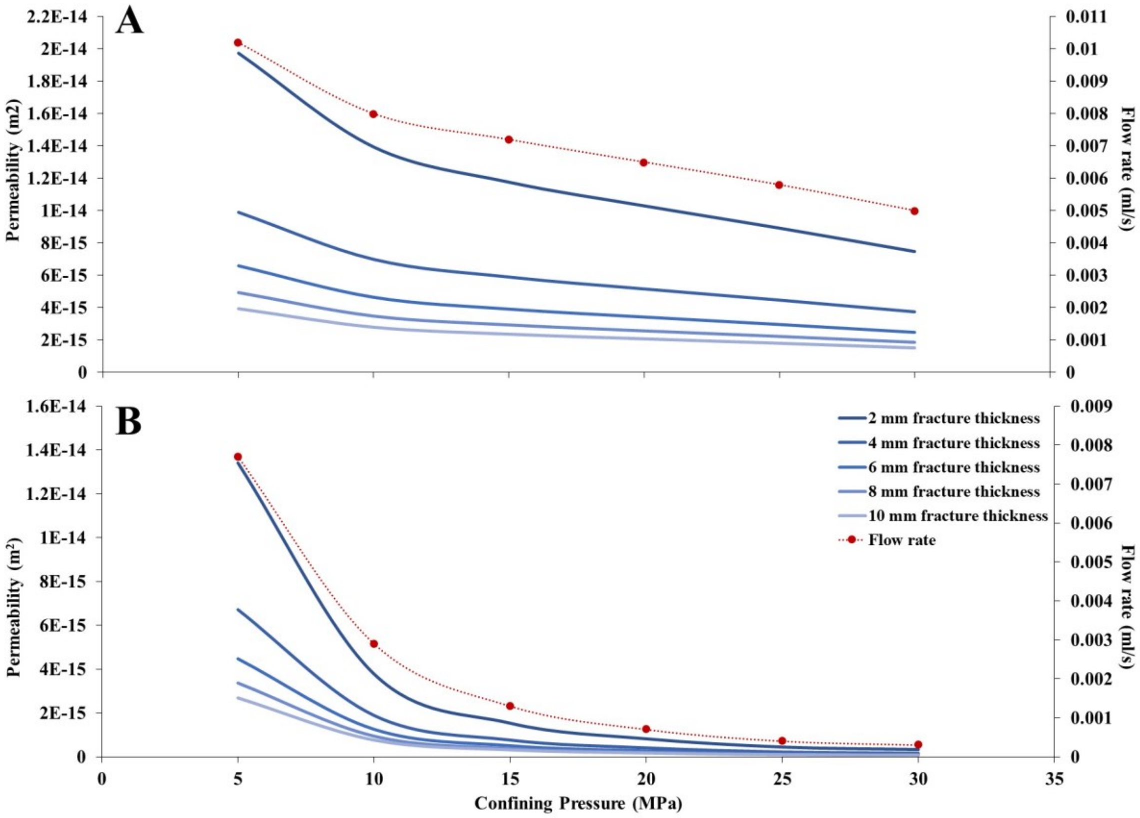

Figure 10. Apparent permeability as a function of effective confining pressure after failure or fracture formation in porous volcaniclastic rock (A) and non-porous andesite sample (B).

High temperature geothermal systems are normally situated in seismically active regions and in volcanic complexes, relying on faults for permeability and abnormally high geothermal gradients (magmatic intrusions) for heat. This, together with resource development activities such as fluid extraction and injection makes such systems dynamic and prone to changes in a relatively short period of time. Fracture network currently being tapped for fluid extraction can experience reduction in permeability, restricting fluid movement. Conversely, previously intact rock can develop secondary permeability through natural faulting and allow fluid migration. We have shown here that such changes in rock and fluid flow properties are reflected in seismic attributes including P and S-wave elastic velocity, bulk and Young's modulus, Lame's coefficient and Poisson's ratio. It is found that high fracture permeability at low confining pressure coincides with significant reduction in seismic attributes except Poisson's ratio. Conversely, reduction in permeability by means of fracture closure and material stiffening results in the lowering of Poisson's ratio but increase in P and S-wave velocities, bulk modulus, Lame's coefficient and Young's modulus. Ultimately, monitoring of these properties with time, using models from surface seismic networks, may be useful in understanding changes in rock and fluid properties in the system and thus allowing for better management of the resource.

Aside from changes in seismic attributes above, we also found that pore fluid pressure release along a conduit (or in this case, fracture plane and damage zone) has a direct effect on seismicity. Fluid extraction in high temperature convective geothermal fields at high temperature conditions is likely to cause changes in the reservoir by pressure reduction that allows formation of two-phase zones and other processes such as infiltration of cold ground water. Based on the gathered data on acoustic emission, seismicity in geothermal fields is also closely linked with fluid extraction processes that allow pore fluid phase change. The pressure recorded in the experiment, around 0.7MPa, correlated to a depth of 800m, is consistent with the geothermal reservoir conditions. Further, seismicity is generated in such process without deformation and fracture movement. Past studies that investigated pore pressure release at elevated temperature in Etna Basalt revealed the AEs generated at venting stage differ from AEs during deformation stage in terms of source mechanism. The former consists mainly of CLVD type events while the latter is dominated by double couple (DC) events produced during shear deformation (Benson et al., 2007). The contribution of injection activities to seismicity is well-established in geothermal fields, albeit in Enhanced Geothermal Systems. This is a likely result of the elevated pore fluid pressure, which then reduces the effective normal stress, locking faults and fractures and thus promotes shear failure. Events are also generated via application of hydraulic pressure in boreholes creating tensile cracks when the minimum horizontal stress is exceeded. However, with the data presented here, it would appear that production activities in high temperature field also contribute to seismicity through processes associated with pore fluids. Although the data on acoustic emission presented here are still incomplete and further data acquisition, processing and analysis are being carried out as of the writing of this paper, it is safe to say that fluid induced seismicity is not limited to injection in high temperature geothermal environments.

We conclude that elastic properties can be utilized to show the state of the medium and to correlate heavily fractured and damaged zones to high permeability, which are key information needed in developing geothermal resources. These seismic attributes are sensitive to changing pressure conditions with time that affect fracture closing and opening. With increasing confining pressure, mimicking increasing depth of burial, we found that fractured rocks exhibit reduction in trend in Poisson's ratio while increases P and S wave velocities, bulk and Young's moduli and the Lame Parameter. This increasing effective confining pressure also coincides with decreasing permeability, in which the rate of reduction is dictated by macro and microstructures present in the material. We conclude further that generating elastic moduli models together with commonly used seismic velocities provides more hints on the state of the medium. For the acoustic emission data, we revealed that pore fluid decompression at high temperature conditions resulting to fluid phase change along a shear damage zone generates events (AE) without fracture movement. This further suggests that pressure reduction in geothermal reservoir that promotes development of two-phase zones has effects on seismicity.

REFERENCES

Ayling, M.R., Meredith, P.G., Murrell, S.A.F.: Microcracking during Triaxial deformation of porous rocks monitored by changes in rock physical properties, I. Elastic-wave Propagation Measurements on Dry Rocks, *Tectonophysics*, **245**, (1995), 205-221.

Baud, P., Meredith, P., Townend, E.: Permeability evolution during triaxial compaction of an anisotropic porous sandstone, *Journal of Geophysical Research*, **117**, (2012), B05203,

Benson PM, Thompson BD, Meredith PG, Vinciguerra S, Young RP. Imaging slow failure in triaxially deformed Etna basalt using 3D acoustic-emission location and X-ray computed tomography, *Geophysical Research Letters*, **34**, (2007), L03303.

Benson, P. M., Vinciguerra, S., Meredith, P.G., Young, R.P.: Laboratory simulation of volcano seismicity, *Science*, **322,** (2008), 249–252.

Benson, P. M., S. Vinciguerra, M.H., Nasseri, Young, R.P.: Laboratory simulations of fluid/gas induced micro-earthquakes: Application to volcano seismology, *Frontiers in Earth Sciences*, **2**, (2014), 32.

Birch F.: The velocity of compressional waves in rocks to 10 kilobars: 1, *Journal of Geophysical Research*, **65**, (1960), 1083-1102.

Blake, O.O., Faulkner, D.R.: The Effect of Fracture Density and Stress State on the Static and Dynamic Moduli of Westerly Granite, *Journal of Geophysical Research: Solid Earth,* **121***,* (2016)*,* 2382-2399.

Bonner, B., Hutchings, L., Kasameyer, P.: A Strategy for Interpretation of Microearthquake Tomography Results in Salton Sea Geothermal Field Based upon Rock Physics Interpretations of State 2 14 Borehole Logs, *Proceedings*, Geothermal Resource Council Annual Meeting, San Diego, California (2006).

Browning, J., Meredith, P., Gudmundsson, A.: Cooling-dominated cracking in thermally stressed volcanic rocks, *Geophysical Research Lett*er, **43**, (2016), 8417–8425.

Castagna, A., Ougier-Simonin, A., Benson, P. M., Browning, J., Walker, R. J., Fazio, M., Vinciguerra, S:. Thermal damage and pore pressure effects of the brittle-ductile transition in Comiso limestone. *Journal of Geophysical Research: Solid Earth*, **123**, (2018).

De Siena L., Thomas, C., Waite, G., Moran, S., Klemme, S.: Attenuation and scattering tomography of the deep plumbing system of Mount St. Helens, *Journal of Geophysical Research*, **119**, (2014a), 8223-8238.

Fazio, M., Benson, P.M., Vinciguerra, S.: On the generation mechanisms of fluid-driven seismic signals related to volcano-tectonics, *Geophys. Res. Lett.,* **44**, (2017).

Faulkner, D.R., Sanchez-Roa, C., Boulton, C., Den Hartog, S.A.M.: Pore Fluid Pressure Development in Compacting Fault Gouge in Theory, Experiments, and Nature, *Journal of Geophysical Research: Solid Earth*, **123, (**2017).

Gehne, S., Benson, P.M:. Permeability and permeability anisotropy in Crab Orchard Sandstone: Experimental insights into spatio-temporal effects, *Tectonophysics*, **712**, (2017), 589-599.

Harnett, C.E., Benson, P.M., Rowley, P., Fazio, M.: Fracture and damage localization in volcanic edifice rocks from El Hierro, Stromboli and Tenerife. *Nature Scientific Report*, **8**, (2018), 1942.

Heap, M.J., Vinciguerra, S., Meredith, P.G.: The Evolution of Elastic Moduli with Increasing Crack Damage during Cyclic Stressing of a Basalt from Mt. Etna Volcano, *Tectonophysics,* **471**, (2009), 153-160.

Hutchings, L., Bonner, B., Jarpe, S., Singh, A.: Micro-earthquake Analysis for Reservoir Properties at the Prati-32 Injection Test, The Geysers, California, *Proceedings*, Fortieth Workshop on Geothermal Reservoir Engineering, Stanford University, Stanford, California (2015).

Ji, S., Sun, S, Wang, Q., Marcotte, D., Lame' Parameters of Common Rocks in the Earth's Crust and Upper Mantle, *Journal of Geophysical Research*, **115**, (2010), B06314.

Julian, B.R., Foulger, G.R.: Improved Methods for Mapping Permeability and Heat Sources in Geothermal Areas Using Microearthquake Data, *Proceedings*, Thirty-Fifth Workshop on Geothermal Reservoir Engineering, Stanford University, Stanford, California (2010).

Julian, B.R., Foulger, G.R., Monastero, F.C., Bjornstad, S.: Imaging Hydraulic Fractures in a Geothermal Reservoir, *Geophysical Research Letters*, **37**, (2010), L07305.

Lockner, D., Byerlee, J., Kuksenko, V., Ponomarev, A., Sidorin, A.: Quasi-static fault growth and shear fracture energy in granite, *Nature*, **350**, (1991), 39-42.

McLaskey, G.C., Lockner, D.A.: Preslip and Cascade Processes Initiating Laboratory Stick Slip, *Journal of Geophysical Research: Solid Earth*, **119**, (2014).

Nara, Y., Meredith, P.G., Yoneda, T., Kaneko, K.: Influence of Macro-fractures and Micro-fractures on Permeability and Elastic Wave Velocities in Basalt at Elevated Pressure, *Tectonophysics*, **503**, (2011), 52-59.

Nasseri, M.H.B., Schubnel, A., Young, R.P.: Coupled Evolutions of Fracture Toughness and Elastic Wave Velocities at High Crack Density in Thermally Treated Westerly Granite, *International Journal of Rock Mechanics and Mining Sciences*, **44**, (2004), 601-616.

Passelègue, F.X., Schubnel, A., Nielsen, A., Bhat, H.S., Deldicque, D., Madariaga, R.: Dynamic Rupture Processes Inferred from Laboratory Microearthquakes, *Journal of Geophysical Research: Solid Earth*, **121**, (2016).

Vinciguerra, S., Trovato, C., Meredith, P.G., Benson, P.M.: Relating seismic velocities, thermal cracking and permeability in Mt. Etna and Iceland basalts. *International Journal of Rock Mechanics & Mining Sciences*, **42**, (2005), 900–910.

Zucca, J.J., Hutchings, L.J., Kasameyer, P.W.: Seismic Velocity and Attenuation Structure of the Geysers Geothermal Field, California. *Geothermics*, **23**, (1994), 111-126.